ARTICLE

A multifunctional flexible sensor based on PI-MXene/$SrTiO_3$ hybrid aerogel for tactile perception

Shihao Deng,[1,2,3] Yue Li,[2,3] Shengzhao Li,[2,3] Shen Yuan,[2,3] Hao Zhu,[2,3] Ju Bai,[2,3] Jingyi Xu,[1,2,3] Lu Peng,[2,3] Tie Li,[1,2,3,4,*] and Ting Zhang[1,2,3,*]

*Correspondence: tli2014@sinano.ac.cn (T.L.); tzhang2009@sinano.ac.cn (T.Z.)

Received: September 20, 2023; Accepted: February 25, 2024; Published Online: February 28, 2024; https://doi.org/10.1016/j.xinn.2024.100596

GRAPHICAL ABSTRACT

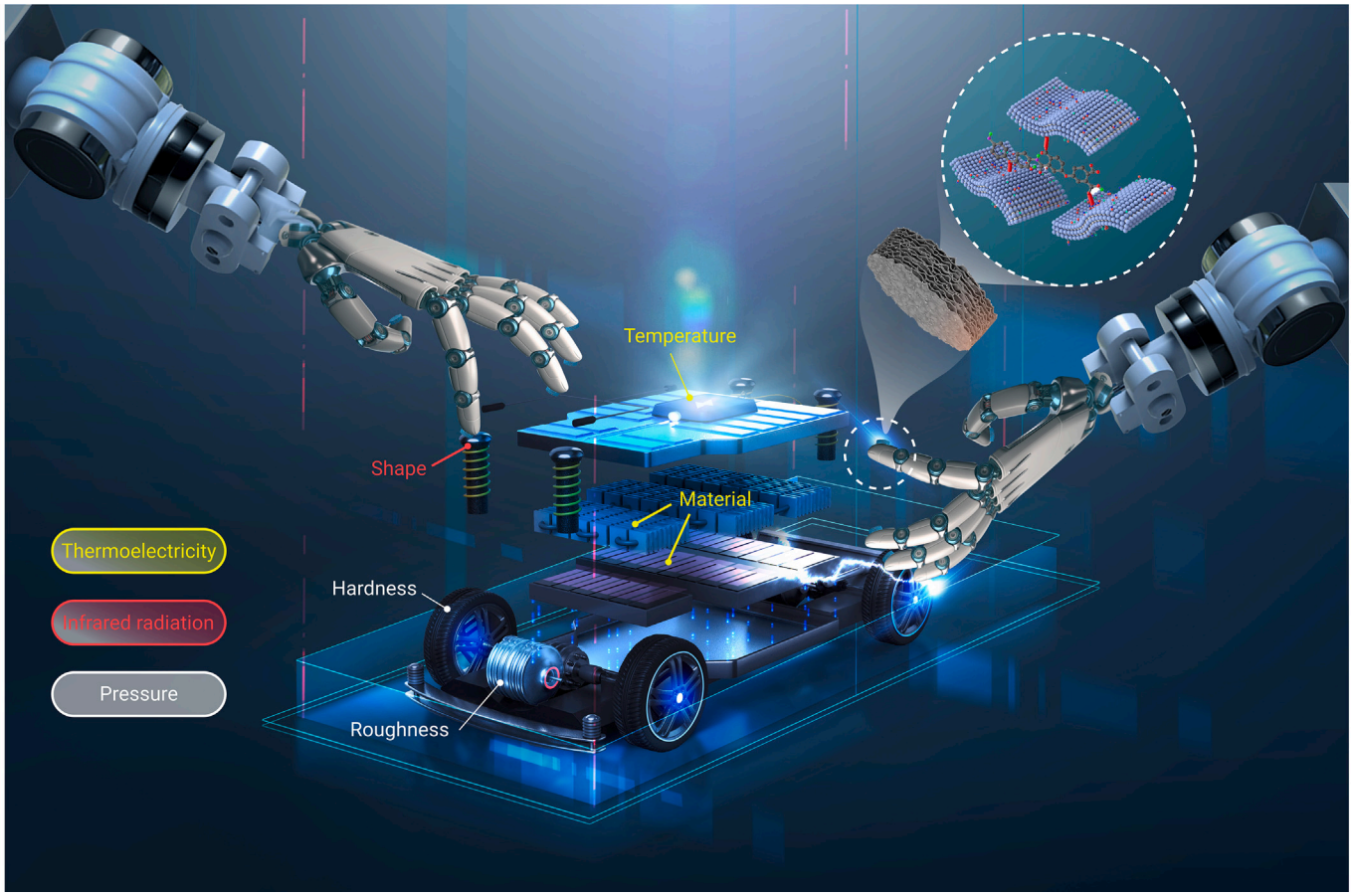

PUBLIC SUMMARY

- The multifunctional tactile sensing function of humanoid robotic arm is seriously lacking.
- This novel composite sensitive aerogel is adaptable to complex environments.
- The new composite aerogel has both system stability and multifunctional sensing function.
- The flexible tactile sensor can realize multifunctional tactile sensing function stably in a complex environment.

ARTICLE

A multifunctional flexible sensor based on PI-MXene/$SrTiO_3$ hybrid aerogel for tactile perception

Shihao Deng,[1,2,3] Yue Li,[2,3] Shengzhao Li,[2,3] Shen Yuan,[2,3] Hao Zhu,[2,3] Ju Bai,[2,3] Jingyi Xu,[1,2,3] Lu Peng,[2,3] Tie Li,[1,2,3,4,*] and Ting Zhang[1,2,3,*]

[1]Nano Science and Technology Institute, University of Science and Technology of China (USTC), Suzhou 215123, China

[2]*i*-lab, Nano-X Vacuum Interconnected Workstation, Key Laboratory of Multifunctional Nanomaterials and Smart Systems, Suzhou Institute of Nano-Tech and Nano-Bionics (SINANO), Chinese Academy of Sciences (CAS), Suzhou 215123, China

[3]School of Nano-Tech and Nano-Bionics, University of Science and Technology of China (USTC), Hefei 230026, China

[4]Jiangxi Institute of Nanotechnology, 278 Luozhu Road, Xiaolan Economic and Technological Development Zone, Nanchang 330200, China

*Correspondence: tli2014@sinano.ac.cn (T.L.); tzhang2009@sinano.ac.cn (T.Z.)

Received: September 20, 2023; Accepted: February 25, 2024; Published Online: February 28, 2024; https://doi.org/10.1016/j.xinn.2024.100596

Citation: Deng S., Li Y., Li S., et al., (2024). A multifunctional flexible sensor based on PI-MXene/$SrTiO_3$ hybrid aerogel for tactile perception. The Innovation **5(3)**, 100596.

The inadequacy of tactile perception systems in humanoid robotic manipulators limits the breadth of available robotic applications. Here, we designed a multifunctional flexible tactile sensor for robotic fingers that provides capabilities similar to those of human skin sensing modalities. This sensor utilizes a novel PI-MXene/$SrTiO_3$ hybrid aerogel developed as a sensing unit with the additional abilities of electromagnetic transmission and thermal insulation to adapt to certain complex environments. Moreover, polyimide (PI) provides a high-strength skeleton, MXene realizes a pressure-sensing function, and MXene/$SrTiO_3$ achieves both thermoelectric and infrared radiation response behaviors. Furthermore, via the pressure response mechanism and unsteady-state heat transfer, these aerogel-derived flexible sensors realize multimodal sensing and recognition capabilities with minimal cross-coupling. They can differentiate among 13 types of hardness and four types of material from objects with accuracies of 94% and 85%, respectively, using a decision tree algorithm. In addition, based on the infrared radiation-sensing function, a sensory array was assembled, and different shapes of objects were successfully recognized. These findings demonstrate that this PI-MXene/$SrTiO_3$ aerogel provides a new concept for expanding the multifunctionality of flexible sensors such that the manipulator can more closely reach the tactile level of the human hand. This advancement reduces the difficulty of integrating humanoid robots and provides a new breadth of application scenarios for their possibility.

INTRODUCTION

Tactile sensing is an important sensory function through which humans have direct contact with the external environment[1]; such sensing encompasses the perception of external physical stimuli (e.g., temperature, pressure, infrared radiation, etc.)[2-5] and the ability of the brain to extract and identify specific information such as roughness, hardness, material, shape, etc.[6-9] In recent years, while humanoid robots have been increasingly developed as intelligent electronic devices, bionic haptic functions have become a key issue for achieving various complex tasks using such robots[10]; thus, the integration of multifunctional flexible tactile sensors has become an important topic[11] because such sensors realize humanoid devices with rich tactile sensing capabilities under conformal conditions.[12,13] Unfortunately, most previously reported flexible tactile sensors only exhibit a single sensing ability or provide similar output patterns for different external signals when attempting to realize multiple sensing functions.[14-16] These tasks require complex circuit design to decouple hybrid output signals completely, complicating the resulting tactile sensing system.[17] These limitations occur because sensitive materials, which are key components of a sensor, have no selective responsiveness. Likewise, the response mechanism attributed to an energy band or a conductive network exhibits similar response profiles when encountering various external signals. Therefore, there is an urgent need to develop novel multifunctional sensitive materials with low coupling and no interference for realizing flexible tactile sensors; in particular, a single device that can realize multiple sensing functions is highly important for realizing lightweight and intelligent equipment with low power consumption.

Specifically, sensitive materials, including polyvinylidene fluoride (PVDF),[2,18] graphene,[19] carbon nanotubes,[20-22] and liquid metals,[15] have been employed to assemble flexible tactile sensors, but these materials usually respond to various signals without selective behavior. For example, most carbon material-based sensors exhibit similar response outputs for temperature and pressure, which leads to difficulties in decoupling sensing signals.[23] In contrast, $SrTiO_3$, as an only temperature-sensitive material with a high thermoelectric coefficient (T_c),[24] possesses an incomparably simple and reproducible way to prepare nanocomposites compared with other bulk thermoelectric materials,[25] which is advantageous for realizing selective multifunction coupling. However, $SrTiO_3$ has a negative T_c and poor conductivity,[26] while other conductive materials currently used have a positive T_c value, increasing the difficulty of modulating the corresponding properties of the derived nanocomposites. In contrast, MXene is a new type of two-dimensional material[27] that exhibits a negative T_c[28] and favorable properties for enhancing the mechanical strength and strain response sensitivity of nanocomposites.[29] Therefore, the combination of $SrTiO_3$ and MXene is hypothesized to maintain synergistic thermoelectric and strain-sensitive performance and then realize the triple sensory functions of force, temperature, and derived infrared radiation. Moreover, the best approach to assemble flexible sensors via thermoelectric materials is to design flexible sensors as porous aerogels with an appropriate thickness for realizing the rapid formation of temperature gradients[30]; this technique can improve the response time and accuracy of devices. However, nanocomposite aerogels derived from two inorganic materials, MXene and $SrTiO_3$ often exhibit relatively low mechanical strength, as previously reported,[31] which can be enhanced by increasing the number of crosslinking points between the internal lamellar nanosheets of aerogels. However, polyimide (PI) is a high temperature-resistant binder that can effectively cause inorganic lamellas to mutually connect with each other by chemical bond crosslinking,[32-34] and this process is expected to lead to the preparation of a high-strength sensitive aerogel. To the best of our knowledge, few studies have reported on sensitive aerogels constructed from the abovementioned MXene, $SrTiO_3$, and PI materials, which can independently sense pressure, temperature, and infrared radiation.

Herer, a novel PI-MXene/$SrTiO_3$ nanocomposite aerogel with a layer-stacked porous structure was prepared. In this composite, PI provides a high-stability skeleton, MXene realizes pressure sensing, and MXene/$SrTiO_3$ achieves both thermoelectric and infrared radiation response behaviors, resulting in high mechanical strength, extra electromagnetic transmission, and thermal insulation to adapt to complex environments. Furthermore, via the pressure response mechanism and the unsteady-state heat transfer principle, this aerogel-derived flexible tactile sensor not only can detect force and temperature in a low cross-coupling manner, but can also sense infrared radiation in a noncontact situation, as shown in Figure 1. Based on pressure sensing and real-time infrared thermal images, the ability of this flexible tactile sensor to distinguish between different roughnesses and hardnesses of objects was demonstrated, as was the ability to distinguish between various materials at different temperatures; moreover, the flexible tactile sensor differentiates among 13 types of hardnesses and four types of materials with accuracies of 94% and 85%, respectively, using a decision tree algorithm. In addition, based on the infrared radiation-sensing function, a sensory array was assembled and shown to successfully recognize different object shapes. These findings demonstrate that this PI-MXene/$SrTiO_3$ aerogel provides a new concept for expanding the multifunctionality of flexible sensors, such that robotic manipulators can more closely realize the tactile performance of human hands.

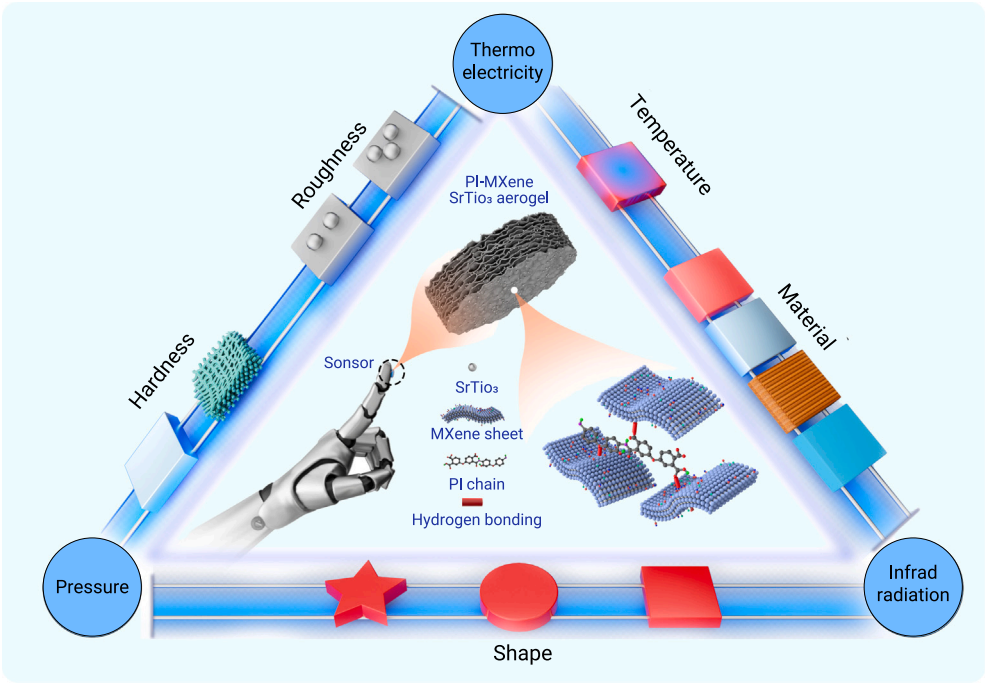

Figure 1. Schematic diagram of a multifunctional flexible tactile sensor based on PI-MXene/$SrTiO_3$ nanocomposite aerogel

RESULTS

Design and characterization of aerogel

The preparation process of the PI-MXene/$SrTiO_3$ sensitive nanocomposite aerogel is shown in Figure 2A. $SrTiO_3$ and MXene were prepared by the solvothermal method and chemical exfoliation, respectively. After thorough mixing of the PI precursor of the polyamide acid/triethylamine (PAA/TEA) mixture, $SrTiO_3$ nanoparticles and MXene dispersion solution, the intended product was achieved via the combined strategy of freeze-drying (aerogel) and heat treatment (PAA converted to PI). A series of characterizations were subsequently performed to verify the morphology and structure of this PI-MXene/$SrTiO_3$ nanocomposite. Compared with the intermediates displayed in Figure S1 (supplemental information), a more orderly stacked porous architecture with dense interfacial crosslinking junctions was formed in the interior of the final product (Figures 2B and 2C), revealing a typical aerogel framework that is favorable for effective mechanical loading and rapid electron transport. As shown in Figure S2, high-quality two-dimensional MXene nanosheets with lateral size of 2 μm and thickness of 5 nm were successfully prepared, and the PI-MXene nanosheets in PI-MXene/$SrTiO_3$ exhibited an increase in thickness of approximately 1 nm after coating with the PI shell. Figures 2D and S3 show that the $SrTiO_3$ nanoparticles are intercalated uniformly in the layers of the PI-MXene nanosheets, as proven by the uniform distribution of Ti, F, C, N, O, and Sr on the two-dimensional lamella and the morphological state of the $SrTiO_3$ nanoparticles in the nanocomposite, which together constitute the enhanced thermoelectric transmission channel. The particle size distribution of the $SrTiO_3$ nanoparticles is also shown in Figure S4, revealing a high size uniformity within 60–90 μm. Moreover, the X-ray diffraction (XRD) pattern of the PI-MXene/$SrTiO_3$ sensitive nanocomposite maintains all the characteristic peaks of $SrTiO_3$ and MXene (Figure 2E), further supporting the favorable crystallinity and structural order of this aerogel. The characteristic peak of MXene is shifted to the left to 6.34°, which indicates that the corresponding interlayer distance increases due to the embeddedness of PI in the MXene interlamination during the composite process.

Furthermore, the chemical structures of the PI-MXene/$SrTiO_3$ aerogel were analyzed, revealing upward shifts in the C=O (1,708 cm^{-1} to 1,720 cm^{-1}), C=C (1,492 cm^{-1} to 1,503 cm^{-1}) and C-N (1,365 cm^{-1} to 1,368 cm^{-1}) absorption peaks of PI (Figure 2F) and an increase in the intensity of the elemental diffraction peaks in this nanocomposite (Figure 2G). The strong interactions between hydrogen and chemical bonds were generated between the functional groups of MXene and the carbonyl groups of the PI chains when heat treatment was applied, which confirmed that PAA-derived PI was employed as the required crosslinking site to enhance the assembly homogeneity and mechanical strength of the three-dimensional aerogel framework. The X-ray photoelectron spectroscopy (XPS) results further prove that, due to the effective protection effect of the PI shell layer, no oxidation of MXene is observed even under thermal treatment at 250°C, as evidenced by the TiO_2 peak in the XPS spectrum of the final nanocomposite (Figure S5) matching that of the original nanocomposite. Based on these findings, the stress performance of the samples with various ratios of PI (P):MXene(M):$SrTiO_3$ (S) was systemically studied, as shown in Figures 2H and S6–S8; it was found that the aerogel with a ratio of P4M2S40 (the aerogel was prepared via the precursor of 4 mL of PAA solution, 2 mL of MXene suspension, and 40 mg of $SrTiO_3$ powder) displayed the optimal compressive strength of 164.47 kPa compared with that of the other samples under the stain of 50%, which can contribute to the transformation of the nonequilibrium crosslinking degree and noncrystalline regions to the equilibrium and mature aerogel network. Specifically, with increasing precursor concentration, the established dynamic crosslinking points (PAA and MXene) and the local nanoenhancement ($SrTiO_3$ and MXene) region in the aerogel matrix were shown to improve the mechanical properties of the final products; however, the performance deteriorated when the precursor content reached a certain threshold, which is attributed to the aggregation of excess precursor hindering the movement of the PI matrix. Moreover, the electrical conductivity and the Seebeck coefficient are generally negatively correlated for most thermoelectric materials, which means that the higher the material conductivity, the lower the Seebeck coefficient.[24] As shown in Figure 2I, the variations in the above two characteristics of the serial nanocomposites are attributed to the increase in the content of $SrTiO_3$, which is mainly caused by the increase in the hot electron transmission path that arises from the uniform dispersion of $SrTiO_3$ in the layers of the MXene until the excessive precursor is aggregated. The values obtained from the P4M2S40 and P4M2S60 samples are essentially equivalent, which is important for enhancing sensory performance. Considering the mechanical strength, the aerogel prepared with a given ratio of P4M2S40 was ultimately chosen for further exploration and application. These enhanced synthetic properties will contribute to the stable development of aerogel-derived flexible sensors. Figure 2J shows the results of the dynamic thermomechanical analysis of the P4M2S40 sample, which revealed that the viscoelasticity of the PI-MXene/$SrTiO_3$ nanocomposite aerogel remained almost unchanged over a wide temperature range from −50°C to 100°C, indicating excellent tolerance to high and low temperatures, which is helpful for the subsequent application of thermoelectric properties. In addition, the extremely low damping ratio (0.025) indicates that the PI-MXene/$SrTiO_3$ nanocomposite has excellent elasticity with low energy loss during dynamic deformation.

Mechanical and thermal shielding properties of the aerogel

Subsequently, we conducted detailed measurements to evaluate the mechanical properties of the PI-MXene/$SrTiO_3$ nanocomposite aerogel under the strain of 0%–50%. Figure 3A shows the stress-strain curves of the PI-MXene/$SrTiO_3$ samples with the optimal ratio at different set strains. These samples can be compressed by sheer forces and quickly return to their initial state after releasing the external compression agent (Figures 3D and S9), exhibiting highly reversible compression under any applied set of strain conditions. In addition, Figure 3B shows that this nanocomposite displays stable stress-strain performance under different compression rates, demonstrating that its mechanical strength is independent of the rate of applied force, which is highly important for aerogel-based flexible sensors to realize practical application. Moreover, the fatigue resistance of the PI-MXene/$SrTiO_3$ nanocomposite during long-term compression was also

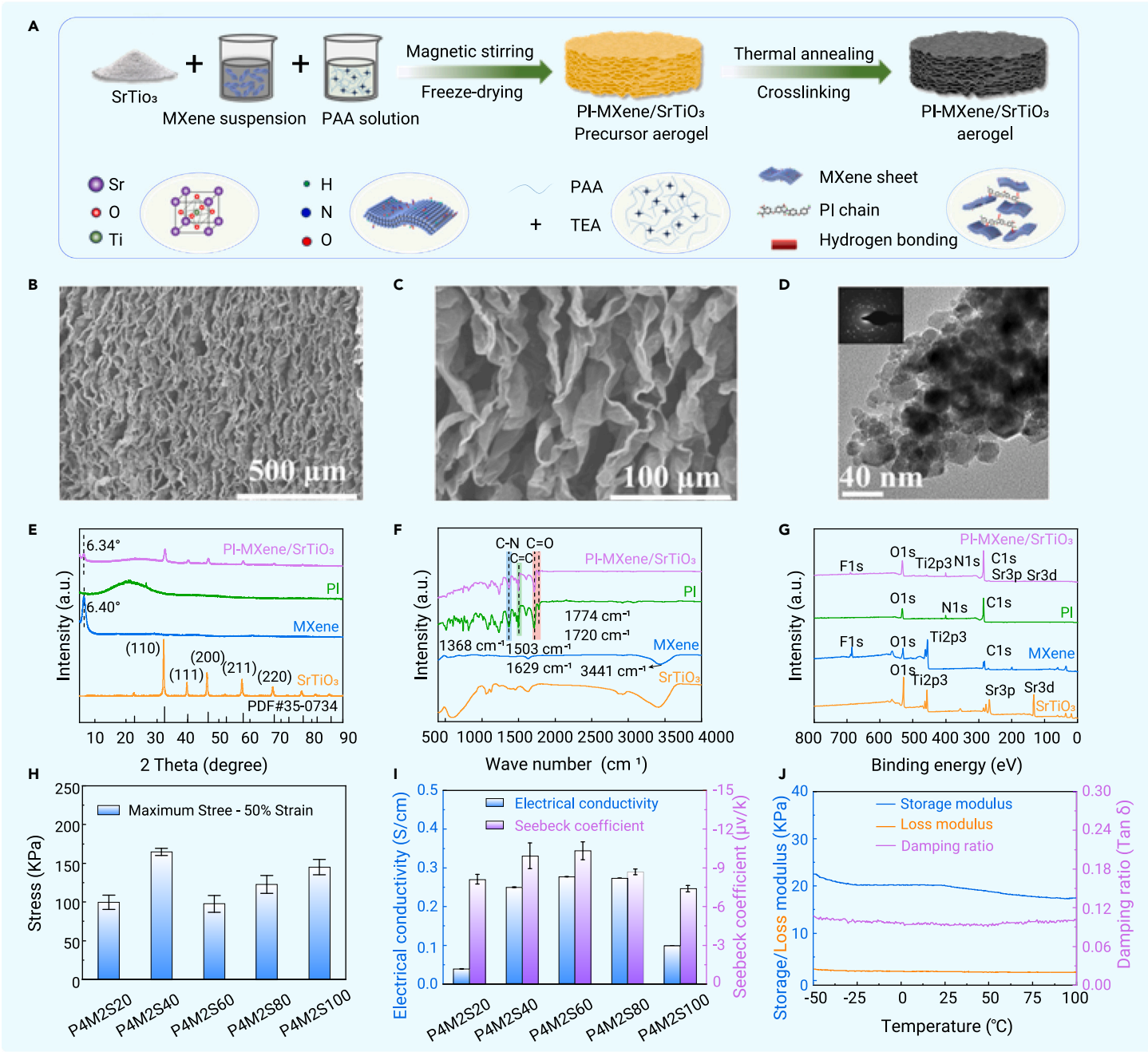

Figure 2. Preparation and characterization of aerogel (A) Flowchart of the preparation process and the morphological (B and C) SEM and (D) TEM characterizations of the PI-MXene/$SrTiO_3$ sensitive nanocomposite aerogel. Structural (E) XRD, (F) FTIR, and (G) XPS analyses of $SrTiO_3$, MXene, PI and the PI-MXene/$SrTiO_3$ aerogel. Comparison of the (H) stress at 50% strain, (I) electrical conductivity and Seebeck coefficient of the PI-MXene/$SrTiO_3$ nanocomposites with different compositions (data are expressed as their means ± SDs ($N \geq 3$)). (J) Dynamic rheological behavior of the P4M2S40 (PAA solution 4 mL, MXene suspension 2 mL, $SrTiO_3$ 40 mg) sample at 1 Hz in the temperature range of −50∼100°C.

tested, and the maximum stress remained almost unchanged after 1,000 compression cycles (Figure 3C). The above results indicate that the as-prepared PI-MXene/$SrTiO_3$ aerogel exhibits favorable structural robustness, superelasticity, and fatigue resistance.

Importantly, in addition to the abovementioned basic requirements for mechanical properties, flexible sensors with features such as heat insulation, waterproofing, and operating suitability, have been increasingly developed, inspiring their expansion into more complex application scenarios. Relatedly, it has been established that aerogels often exhibit favorable environmental suitability. Here, the thermal insulation and electromagnetic transmission performance of this PI-MXene/$SrTiO_3$ nanocomposite aerogel were studied, as shown in the schematic diagram in Figure 3E. Generally, MXene-based nanocomposites have a strong electromagnetic shielding effect; however, bionic robots need to communicate through electromagnetic waves in some cases. Moreover, if the robot manipulator exhibits a strong electromagnetic shielding effect, this shielding will interfere with the normal use of the robot. As shown in Figures 3F and S10, the PI-MXene/$SrTiO_3$ nanocomposite aerogel exhibits a very low shielding effect on the full bands, especially for commonly used communication control frequencies such as those in the 2.4 GHz range, with an average electromagnetic loss as low −20 dB, which signifies that the commonly used communication wave can pass through the aerogel and does not weaken the signal significantly. This effect is very different from the electromagnetic shielding effect of other reported MXene-based composites and has positive implications for our prepared materials for application in robotics. In addition, the PI-MXene/$SrTiO_3$ nanocomposite aerogel also has excellent thermal insulating performance, as shown in Figures 3G and S11. The *in situ* temperature survey revealed that the difference between the finger spaced with the aerogel and the other finger directly touching the hot plate ranged from 16°C to 19°C after 120 min. As the hot plate and the thermal insulation

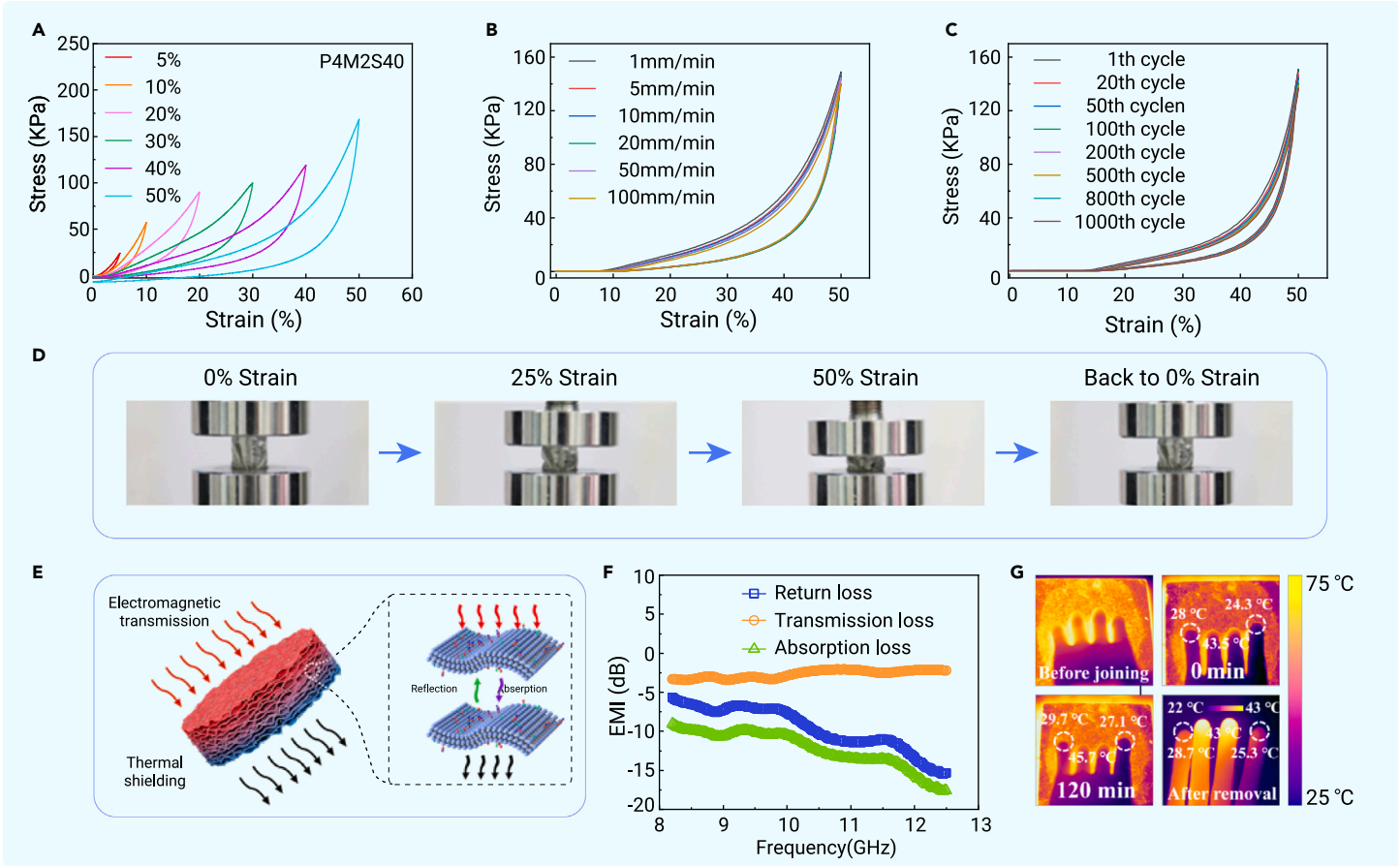

Figure 3. Compression mechanics, electromagnetic transmission, and thermal insulation properties of aerogel Stress-strain (σ-ε) curves of the PI-MXene/$SrTiO_3$ sensitive nanocomposite aerogel at different (A) set strains and (B) compression velocities. (C) Stability curves of the aerogel with the optimal ratio tested at 50% strain for 1,000 compression cycles. (D) Digital photographs of the nanocomposite compressed to 50% and back to its original state. (E) Schematic diagram of the electromagnetic transport and thermal insulation of the PI-MXene/$SrTiO_3$ aerogel, as well as its practical electromagnetic performance (F) and (G) images of thermal insulation at different times.

aerogel were removed, the temperature difference between the fingers also maintained within the range of 14°C–18°C. This excellent thermal insulation can facilitate the output of high-quality thermoelectric signals, because the device can intrinsically develop a higher temperature gradient in proximity to an external heat source.

Pressure-sensing performance of flexible sensors

The piezoresistive sensing performance of the multifunctional flexible tactile sensor derived from the as-prepared PI-MXene/$SrTiO_3$ nanocomposite aerogel was systematically investigated, as shown in Figure 4. The sensing mechanism in Figure 4A demonstrates that the change in the piezoresistive resistance of this flexible sensor is mainly attributed to variations in the contact area with compressive deformation, which shows excellent response to various compressive strains and corresponding pressures ranging from 0% to 50% and 0–26.2 N with high discrimination, as shown in Figures 4B and S12. The corresponding relation of the resistance changes ($\Delta R/R_0 = (R - R_0)/R_0$, where R and R_0 represent the values of instantaneous and initial resistance, respectively) to compressive strains is revealed in Figure 4C, where two particular sensing ranges can be clearly observed. At initial compressive strains of 0%–10%, the construction of new conductive networks results in an exponential decrease in resistance. When the compressive strain is further increased to 50%, the contacts between neighboring MXene nanosheet layers increase synchronously and the compressive strain tends to decrease rapidly and linearly, leading to the highest sensitivity throughout the compression process. In general, the strain sensitivity of the sensor is evaluated using a gauge factor ($GF = (\Delta R/R_0)/\varepsilon$, where ε is the applied strain), which is calculated to be 1.37 in the linear strain range. The response time is also an important index for the sensor. At an instantaneous strain of 1%, the response time is 0.4 s, and the recovery time is 0.3 s, as shown in Figure 4D. Moreover, the cycling performance of the flexible tactile sensor under various compression strains (Figure 4E) and rates (Figure 4F) was also explored, the flexible tactile sensor exhibited high cycling stability and repeatability at each stage of strain and rate, indicating that this device can be employed to detect both small and high external strains or pressures without affecting compression rates, which is consistent with the results obtained from Figures 3A and 3B. Overall, the multifunctional flexible sensor based on the PI-MXene/$SrTiO_3$ aerogel possesses excellent piezoresistive sensing performance.

The proposed PI-MXene/$SrTiO_3$ aerogel-derived multifunctional flexible tactile sensor was initially designed to utilize two sensing mechanisms (based on piezoresistive and thermoelectric effects) to sense compression and temperature. It has been shown that low cross-coupling between various sensory functions is highly important in such applications; therefore, the influence of temperature on the piezoresistive behavior of the proposed device was also studied. As shown in Figures 4F and 4G, the resistance of the flexible sensor varies minimally with increasing temperature up to a wide range of 0–25 K, regardless of whether the device is subjected to a dynamically increasing pressure (Figure 4G; in particular, an extracted representative set tested under a pressure of 8 N is shown in Figure S17) or a continuously constant pressure of 0–12 N (Figure 4H), completely confirming that the piezoresistive performance is negligibly disrupted by temperature interference. In addition, a long cyclic compression test was conducted to verify the fatigue resistance of the flexible sensor (Figure 4I), which exhibited excellent high stability after more than 1,000 cycles at a strain of 15%.

Thermoelectric sensing characteristics of flexible sensors

In addition to the piezoresistive sensing properties, this multifunctional flexible tactile sensor has thermoelectric sensing capabilities. A unique feature of this study is that two identical types of active materials—MXene and $SrTiO_3$—with negative thermoelectric coefficients were simultaneously chosen to prepare the nanocomposite aerogel, thereby enabling the direct conversion of

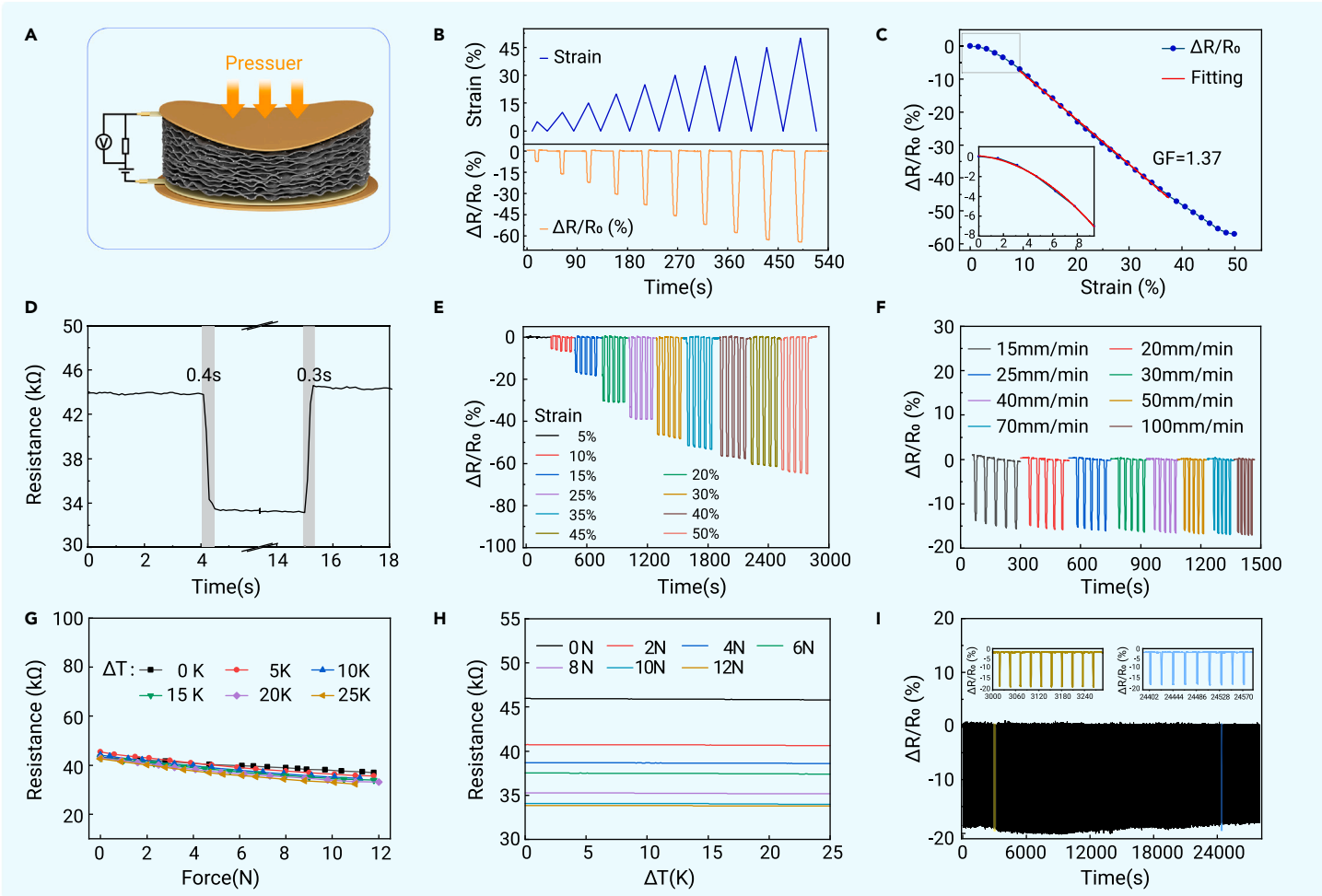

Figure 4. Piezoresistive sensing performance of the sensor (A) Schematic diagram of the piezoresistive effect of the multifunctional flexible tactile sensor derived from the PI-MXene/$SrTiO_3$ nanocomposite aerogel. (B) Stepwise piezoresistive sensing behavior of the flexible sensor up to a strain of 50%. (C) Relation of $\Delta R/R_0$ to compressive strain and (D) the response time of the flexible tactile device. Piezoresistive sensing performance of the flexible tactile sensor at (E) different compressive strains (compression speed of 15 mm min^{-1}) and (F) various compression speeds under a strain of 15%. (G and H) Plots of the influence of temperature on the piezoresistive behavior of this multifunctional device. Temperature coupling effects have a negligible effect on the piezoresistive response. (I) The stability of the flexible sensor after being cycled more than 1,000 times at a strain of 15%.

thermal and electrical energy without the counteraction of migratory electrons, which achieved an enhanced thermoelectric coefficient, as shown in Figure 2I. According to the Seebeck effect, the thermoelectric open-circuit voltage is calculated as follows:

$$\Delta U = S_T \times \Delta T \qquad \text{(Equation 1)}$$

where S_T is the Seebeck coefficient and ΔT is the temperature gradient. Therefore, as illustrated in Figure 5A, because of the synergetic thermoelectric nature of the components in the PI-MXene/$SrTiO_3$ nanocomposite, the carriers undergo significantly enhanced thermal diffusion when ΔT is applied, generating a considerable output voltage that demonstrates, an excellent linear response to ΔT values ranging from 0 to 25 K; this response range covers commonly used temperature conditions, and is shown in Figure 5B. Combined with the results shown in Figure S13, the Seebeck coefficient (−11.76 μV/K) of PI-MXene/$SrTiO_3$ is greater than that (−4.95 μV/K) of PI-MXene. Figure S14 shows the effect of different thicknesses on the piezoresistive and thermoelectric properties of the as-obtained flexible tactile sensor. The thickness has no effect on the piezoresistive response. However, the greater the thickness, the greater the Seebeck coefficient of PI-MXene/$SrTiO_3$. A thickness of 9 mm was chosen as the best parameter since the as-prepared samples were so hardened because of the excessive contraction of the aerogel over the above optimal thickness. More importantly, the thermoelectric voltages of the sensor show the same output trends under any of the conditions of several identical ΔTs vs. various applied forces (Figure 5C, under a fixed ΔT with increasing pressure.) or several constant pressures vs. various ΔT (Figure 5D, under a fixed pressure with different ΔT), revealing that the outputs of the device are inherently insensitive to the variation in applied pressure. Therefore, considering the abovementioned piezoresistive properties, it is clear that no cross-coupling response occurred between the temperature and pressure response, further verifying the multifunctional interference-free sensing ability of this flexible tactile sensor based on the PI-MXene/$SrTiO_3$ nanocomposite. A multiphysical field simulation was employed to further investigate the cross-coupling behavior between the temperature and pressure for this device. As shown in Figure S15, the output voltage of the flexible sensor remains stable and is not affected by pressure stimuli under a given temperature gradient, which is consistent with practical results. However, under different temperature gradients, the piezoresistive sensing performance of the sensor is not affected either, and its piezoresistive sensing curves overlap (Figures S16 and S17). The response times of the flexible sensor were also measured at a ΔT of 20 K (Figure 5E), which yielded a response and recovery time of 2.4 s and 11.6 s, respectively. Moreover, because of its thermoelectric sensing character, this multifunctional flexible sensor naturally possesses the noncontact sensing capability, as shown in Figure 5F. Like in contact mode, when the heat source is present at a distance, it can also conduct heat to the surface of the thermoelectric device and subsequently generate an output voltage via ΔT, as illustrated in Figure 5G. The differences between the noncontact signals were further explored at various distances and ΔT ranges of 0–20 mm and 0–25 K, as shown in Figures 5H and S18, revealing the linear change trends of the open-circuit voltages, which decrease with increasing distance under the same ΔT and increase with increasing ΔT under the same distance. This may occur because the ΔT values between the upper and lower electrodes change with respect to the variation in the distance or ΔT, which results in varying output voltages.

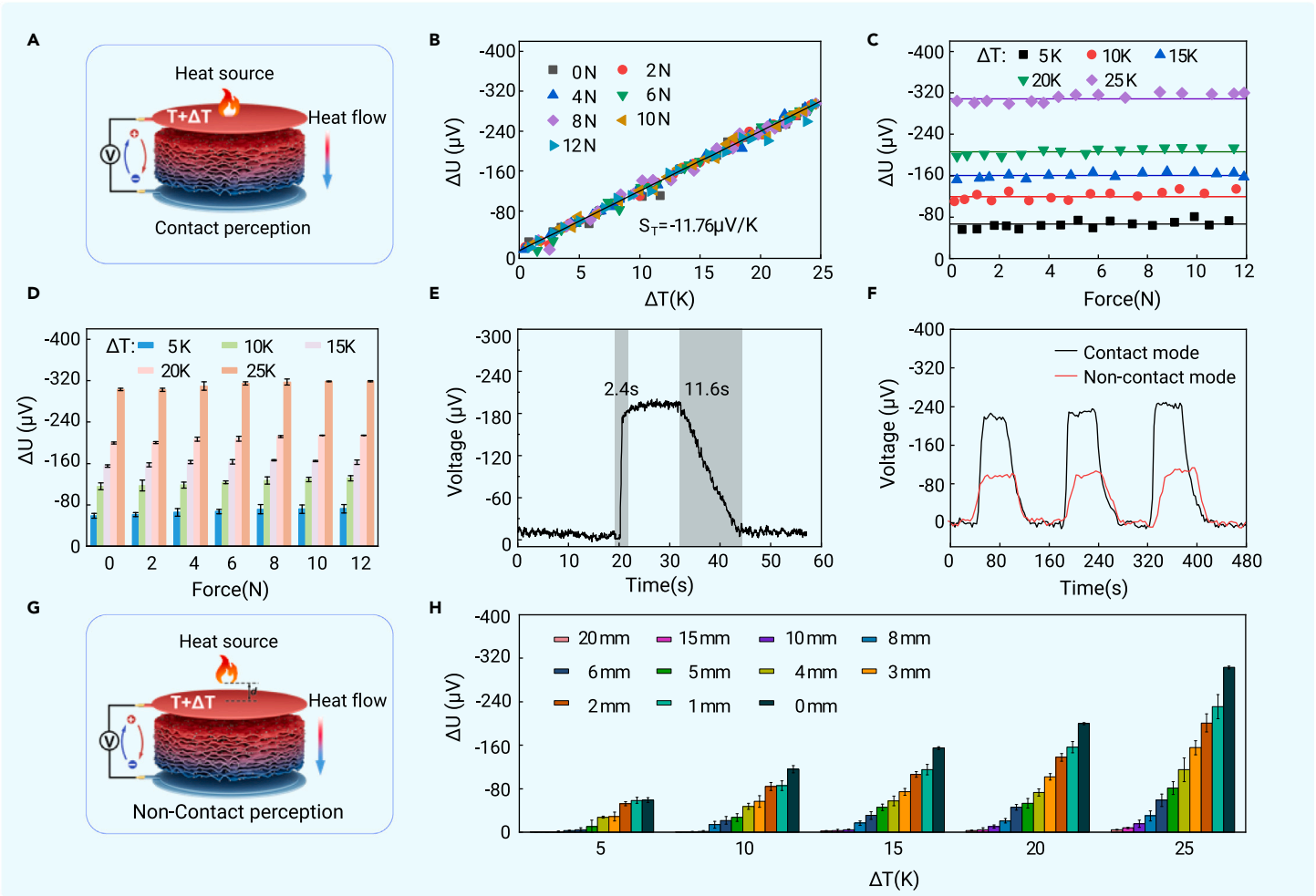

Figure 5. Thermoelectric sensing performance of the sensor (A) Schematic diagram of the thermoelectric effect of the PI-MXene/$SrTiO_3$-based multifunctional flexible tactile sensor. (B and C) Plots of the output voltages of the flexible sensor vs. the variations in temperature and force. (D) The output voltages of the flexible device are tested under external pressure by fixing an external temperature difference (data are expressed as their means ± SDs (N ≥ 3)). (E) Response and recovery time of the flexible sensor under a temperature difference of 20 K. (F) Comparison of the contact and noncontact modes of the output thermoelectric signals under the same heat source with a temperature difference of 20 K, where the noncontact distance is 3 mm. (G) Schematic diagram of the noncontact sensing mode of the multifunctional flexible sensor, and (H) its output voltages under different temperature gradients for various distances between the heat source and the device (data are expressed as their means ± SDs (N ≥3)).

Infrared radiation-sensing property of flexible sensors

In addition, infrared radiation is another temperature-dependent characteristic of objects. Based on Stephen-Boltzmann (Equation 2) and the energy decay (Equation 3):

$$I_0 = \varepsilon \times \sigma \times T^4 \times S \qquad \text{(Equation 2)}$$

where ε is the object's emissivity, which is determined by the nature of the object's surface. σ is the Stephen-Boltzmann constant, with a value of 5.67 × 10^{-8} W/(m^{-2}·K^4). T is the temperature of the object. S is the area of the object that emits infrared radiation:

$$I = \frac{I_0}{d^2} \qquad \text{(Equation 3)}$$

where I_0 is the infrared radiation intensity when the distance (d) between two objects is 0. The associative result can be calculated as follows (Equation 4): The intensity of infrared radiation emitted by an object is determined only by its own temperature when the shape is given:

$$I = \frac{\varepsilon \times \sigma \times T^4 \times S}{d^2} \qquad \text{(Equation 4)}$$

thus, for its temperature response ability as shown in Figure 5, the PI-MXene/$SrTiO_3$ aerogel-based multifunctional flexible tactile sensor can also sense the infrared thermal radiation released from different objects in addition to the above piezoresistive and thermoelectric sensing modes, as shown in Figure 6A. In this experiment, to verify this novel feature of the multifunctional sensor, a systemic test was conducted. Figure 6B shows that, when the temperature of the stainless steel sample was fixed 1 mm from the sensor, it was heated from 305 K to 325 K at a fixed distance of 1 mm from the sensor, and the output signals of the device increased with increasing intensity of the infrared radiation of the object. Correspondingly, the output signals of the sensor decreased as the setting distance increased from 1 mm to 5 mm under constant infrared radiation from the object (320 K), as shown in Figure 6C. Moreover, three objects with different emissivities (stainless steel, PVC plastic board, and plywood board) were further chosen to investigate the identification accuracy of this thermoelectric aerogel-based flexible sensor. The differences between the infrared radiation of the different objects are accurately reflected in the output signals of the multifunctional sensor, regardless of whether the samples were excited at the same temperature (320 K) at different distances (Figure 6D) or at the same distance (1 mm) at various temperatures (Figure 6E), clearly revealing the high sensitivity of the response to infrared thermal radiation.

Roughness and hardness recognition of the multifunctional sensor

Therefore, with previously reported flexible sensors, the proposed PI-MXene/$SrTiO_3$ aerogel-based multifunctional flexible tactile sensor exhibits the optimal comprehensive properties of piezoresistive, thermoelectric, and infrared radiation response behaviors (Table S1, supporting information). Thus, in order to demonstrate the practical applications of this flexible sensor, the device was assembled on the finger of a humanoid robot to sense pressure and roughness. As shown in Figure 7A, the flexible sensor can detect the exact state of contact, which is an

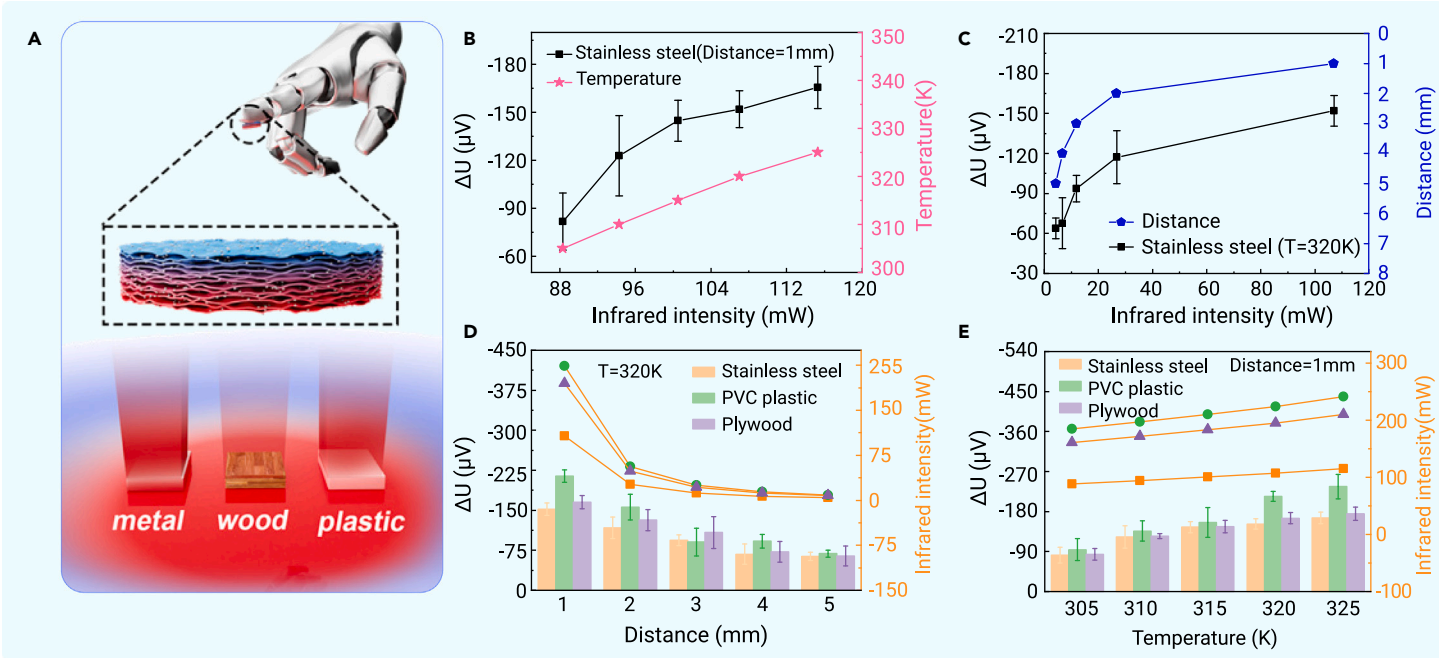

Figure 6. Infrared radiation-sensing performance of the sensor (A) Schematic diagram of the infrared radiation response of the PI-MXene/$SrTiO_3$ aerogel-based multifunctional flexible tactile sensors. The output signals of the sensor change along with the intensity of infrared radiation when the sample of stainless steel (area of 400 mm^2) is (B) 1 mm away from the device at a temperature range of 305–325 K, and (C) 1–5 mm away from the device at a constant temperature of 320 K. The output signals of the flexible sensor when the stainless steel, PVC plastic plate, and plywood plate are used are (D) gradually close to the device at a constant temperature of 320 K, and (E) at a temperature range of 325 K at a constant distance of 1 mm (data are expressed as theri means ± SDs (N ≥ 3)).

important issue when evaluating the grab state of objects. To demonstrate the practical application of the aerogel-based multifunctional flexible sensor in more complex situations, the device was placed under the conditions of simultaneous changes in pressure and temperature, and the piezoresistive sensing performance showed stable sensing behaviors under different temperature differences (Figure S19). In addition, the multifunctional sensor can also recognize the roughnesses formed by different Braille patterns, as shown in Figure 7B. When sliding over the board, the sensor can detect the different contact strains caused by the Braille patterns with different roughnesses via variational output waveforms, which can be leveraged to enrich the sensing capabilities of the robots. In addition, pressure sensing-derived hardness recognition is important for expanding the range of applied intelligent equipment, such as robots. The mechanism of hardness recognition is as follows. When objects with different hardnesses apply the same strain to the sensor, the forces acting on the device will be different, which will result in differences in the output signals. For example, an object with a higher hardness exerts more pressure on a flexible sensor, which results in a larger change in resistance. Moreover, machine learning algorithms, which are powerful tools for sensitively distinguishing small differences in response curves and classifying them accordingly, were further used to extract the instinctive properties of objects[35-38] Here, 13 types of materials with various hardnesses were selected for discrimination testing, as shown in Figure 7C. When processing the identifying data, the flexible tactile sensor touched each type of substance 100 times at a constant time (5 s), and a large amount of data was recorded at a frequency of 10 Hz. To better align the individual data, the first 5 s and the last 10 s of the data were intercepted using the peak of the curve as a reference point, so that the total duration of each time series was 15 s, as shown in Figures 7D and S20; subsequently, 1,000 identical (15 s) time series data were collected for each substance. The dataset was then divided into 800 training instances and 200 test instances. As an interval-based classifier, a decision tree classifier was chosen to learn the features embedded in the data. Finally, an average accuracy of 94% was achieved for material recognition by this PI-MXene/$SrTiO_3$ aerogel-based flexible sensor, as shown in the confusion matrix in Figure 7E.

Material and shape recognition of the multifunctional sensor

Based on the thermoelectric sensing ability of the flexible tactile sensor, the device can be used to recognize the outside temperature, as shown in Figures 8A and 8B, which can realize the function of high temperature warning. Additionally, the practical performance of the flexible tactile sensor was demonstrated in more complex situations involving simultaneous changes in pressure and temperature, and the thermoelectric sensing performance was equally stable under different pressures and strains (Figure S21). Moreover this multifunctional flexible tactile sensor also has a skin-like function for categorizing a number of materials. As the thermal conductivity of individual materials varies greatly, different types of materials feel differently on the skin. For example, because metals are good thermal conductors, skin contact with metals will be colder or hotter than contact with other materials at the same temperature. Inspired by the sensory properties of skin, we demonstrated that the change in open-circuit voltage caused by unstable heat conduction is closely related to the thermal conductivity of a material and can be used to distinguish between different substances. Here four types of materials with different heat transfer capabilities, namely metal, wood, plastic, and ceramic materials, were selected and cut into the same dimensions, as shown in Figure 8D. A hot plate was assembled at the bottom of the sensor, the temperature was set to 75°C, and an infrared thermography camera was subsequently used to record the temperature changes when the sensor contacted the objects heated to the same temperature. After the device touches the object, heat from the object is quickly transferred to the sensor. In response, the open-circuit voltage increases with ΔT between the upper and lower sides of the sensors. As shown in Figure 8C, after maintaining the heat for 3, 5, 10, and 30 s, we observe the heat transfer from the four objects to the sensor. The interface of the device in contact with the metal has a higher temperature at the top of the device than that of the sensor in contact with the wood, plastic, and ceramic materials, indicating that the metal block transfers more energy to the sensor than others at the same time. The heat transfer capacities of the ceramic, plastic, and wood board decrease in that order. Based on previous work,[39] the effect of the intrinsic properties of an object on the unsteady heat transfer process has been explored:

$$\frac{\Delta T_1}{\Delta T_2} = \frac{\sqrt{\rho_2 c_2 \lambda_2}}{\sqrt{\rho_1 c_1 \lambda_1}} \quad \text{(Equation 5)}$$

where λ is the thermal conductivity, ρ is the density, c is the specific heat capacity, and ΔT is the temperature gradient. Specifically, ΔT_1 and ΔT_2 are the direct temperature differences between different objects and the sensor. In addition, ρ_1 and ρ_2, c_1 and c_2, and λ_1 and λ_2 are the intrinsic property parameters of various

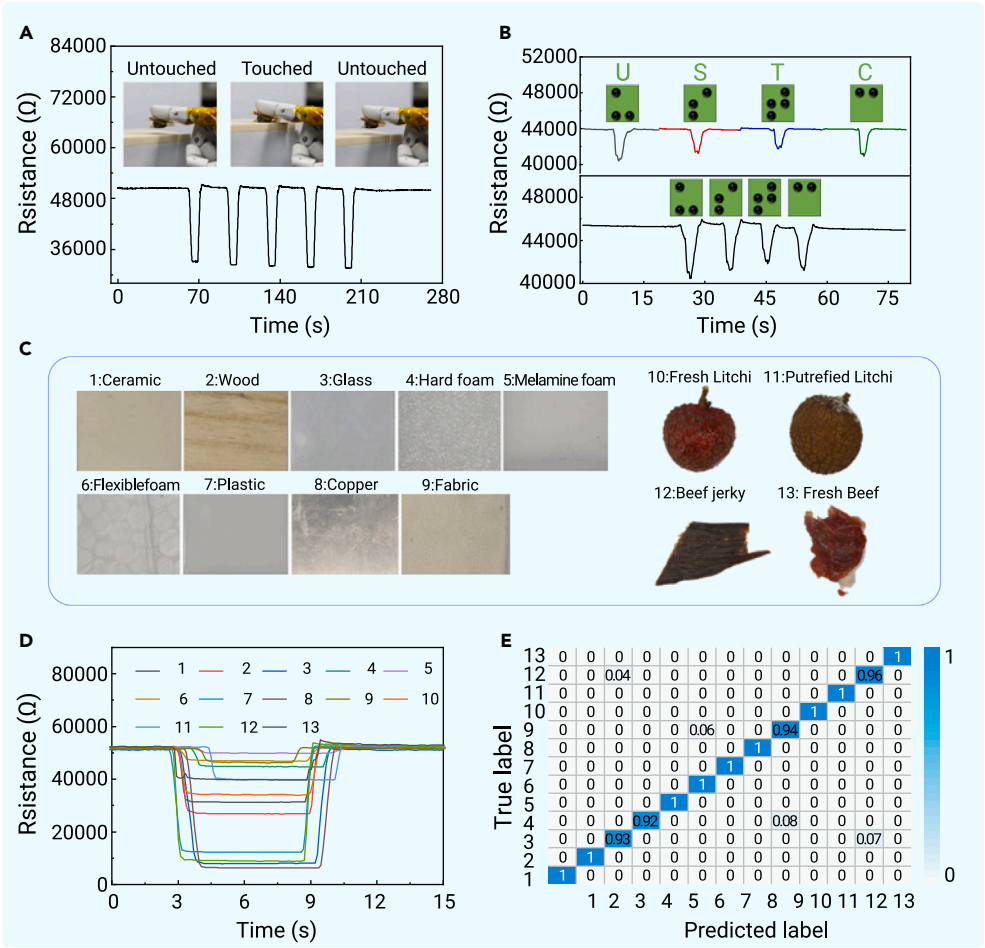

Figure 7. Application demonstration of piezoresistive sensing performance based on sensor Recognition of the (A) touching status and (B) roughness of the multifunctional flexible tactile sensor. (C) Photographs of objects used for hardness recognition. (D) Comparison of the sensing waveforms when the device touches the objects with different hardnesses. (E) Confusion matrices for the results of hardness recognition from the decision tree model.

objects. Therefore, ΔT is determined by the intrinsic property of the objects themselves. Because the ΔT of the contact surface between the objects and the sensor is $\Delta T_{Copper} > \Delta T_{Ceramic} > \Delta T_{Plastic} > \Delta T_{Wood}$, substituting the Seebeck effect formula: $\Delta U = S_T \times \Delta T$, the order of the maximum output voltage is $\Delta U_{Copper} > \Delta U_{Ceramic} > \Delta U_{Plastic} > \Delta U_{Wood}$. This result signifies that the maximum value of the output voltage is closely related to the object's λ, ρ and c. Therefore, the sensor has the ability to recognize materials within a certain range. Similarly, machine learning has been employed to assist flexible sensors in material recognition.[40-42] Here, the device touched each type of material 100 times at a constant time (30 s) and a large amount of data was recorded at a frequency of 2 Hz. To better align the individual data, the first 100 s and the last 150 s of the data were intercepted using the peak of the curve as a reference point, so that the total duration of each time series data point used for training was 250 s, as shown in Figure 8E. As an interval-based classifier, a decision tree classifier was chosen to learn the features embedded in the data. Finally, the average accuracy of material recognition reaches 85%, as shown in the confusion matrix in Figure 8F.

Furthermore, the function of shape recognition was also demonstrated based on the infrared radiation-sensing characteristic of this multifunctional flexible tactile sensor. As shown in Figure 8G, a sensory array was designed and prepared by employing the flexible sensor as a unit, and a PVC plastic sheet was cut into three shapes, square, parallelogram, and triangle, which fixed their temperature at 320 K. When the devices were brought close to the sensory array by approximately 1 mm, the flexible array could generally recognize the above three shapes (Figure 8H) by mapping the specific response data of each unit, as shown in Figure S22.

DISCUSSION

In this study, a novel PI-MXene/$SrTiO_3$ nanocomposite aerogel was prepared, in which PI provides a high-stability skeleton, MXene realizes the pressure-sensing function, and MXene/$SrTiO_3$ realizes the thermoelectric and infrared radiation response behaviors together, displaying high mechanical strength, efficient thermal insulation, and reliable electromagnetic transmission. Thanks to the thermoelectricity and conductivity of MXene/$SrTiO_3$, the aerogel-derived flexible sensor has the ability to sense external forces and ambient temperature through detecting the change of resistance and open-circuit voltage with low cross-coupling manner. In addition, the sensor also has the ability to sense the different intensities of infrared thermal radiation. Subsequently, it was experimentally demonstrated that this multifunctional flexible sensor can recognize 13 different hardness objects (with 94% accuracy) and four different materials (with 85% accuracy) via a decision tree algorithm. Finally, a sensory array was assembled and realized the object shape recognition. We envision that this multifunctional flexible tactile sensor based on PI-MXene/$SrTiO_3$ nanocomposite aerogel can enrich the sensing information and provide as much and accurate tactile information as possible to the robotic manipulator.

MATERIALS AND METHODS

See the supplemental information for details.

REFERENCES

1. Raspopovic, S., Valle, G., and Petrini, F.M. (2021). Sensory feedback for limb prostheses in amputees. Nat. Mater. ***20***(7): 925–939. https://doi.org/10.1038/s41563-021-00966-9.
2. Zhu, P., Wang, Y., Wang, Y., et al. (2020). Flexible 3D Architectured Piezo/Thermoelectric Bimodal Tactile Sensor Array for E-Skin Application. Adv. Energy Mater. ***10***(39). https://doi.org/10.1002/aenm.202001945.
3. Xu, J., Sun, X., Sun, B., et al. (2023). Stretchable, Adhesive, and Bioinspired Visual Electronic Skin with Strain/Temperature/Pressure Multimodal Non-Interference Sensing. ACS Appl. Mater. Interfaces ***15***(28): 33774–33783. https://doi.org/10.1021/acsami.3c07857.
4. Xiao, H., Li, S., He, Z., et al. (2023). Dual Mode Strain–Temperature Sensor with High Stimuli Discriminability and Resolution for Smart Wearables. Adv. Funct. Mater. ***33***(16). https://doi.org/10.1002/adfm.202214907.
5. Wei, X., Wang, B., Wu, Z., et al. (2022). An Open-Environment Tactile Sensing System: Toward Simple and Efficient Material Identification. Adv. Mater. ***34***(29): e2203073. https://doi.org/10.1002/adma.202203073.
6. Wang, H.L., Chen, T., Zhang, B., et al. (2023). A Dual-Responsive Artificial Skin for Tactile and Touchless Interfaces. Small ***19***(21): e2206830. https://doi.org/10.1002/smll.202206830.

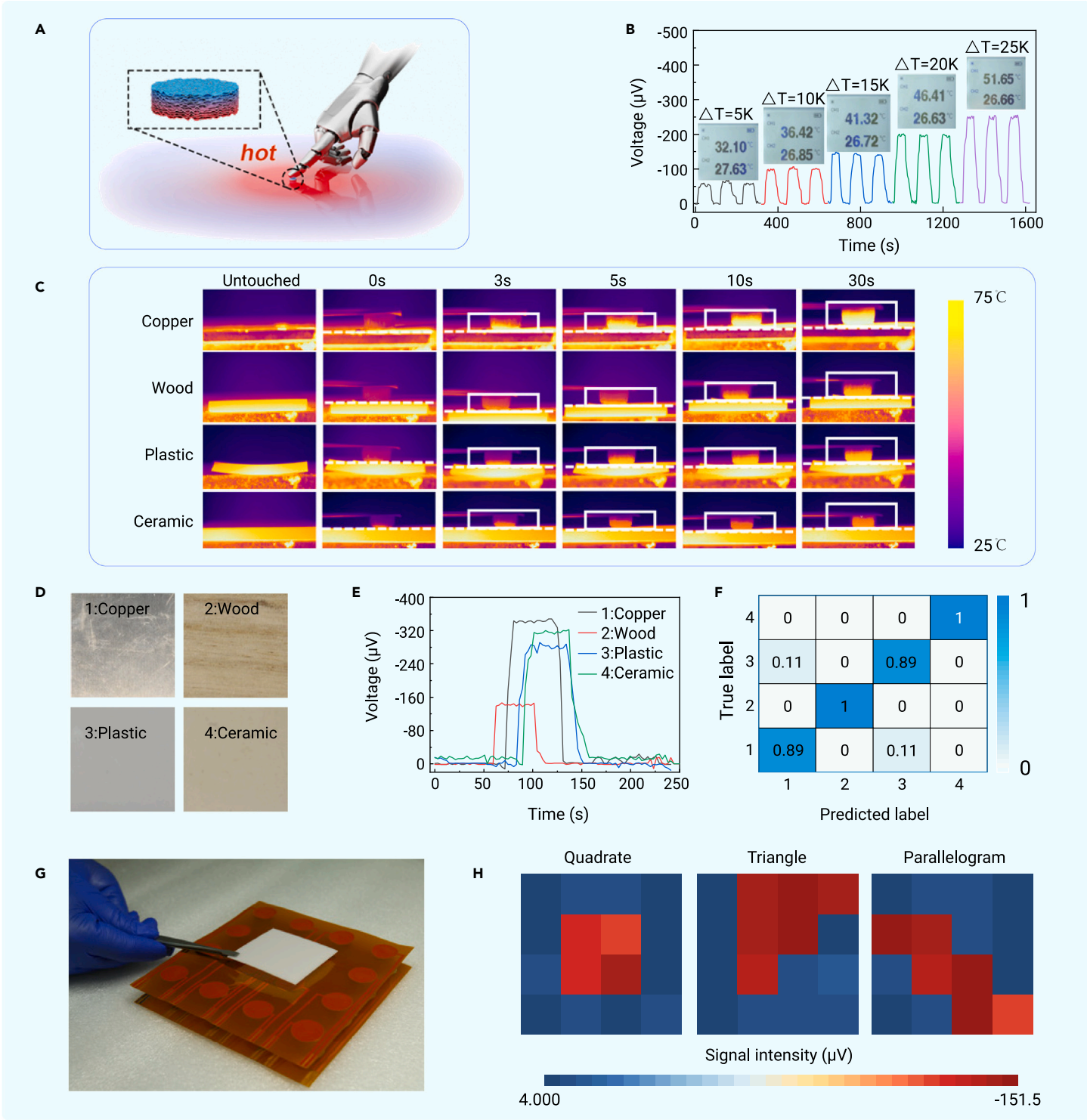

Figure 8. Application demonstration of sensor sensing performance based on thermoelectric and infrared radiation (A) Schematic diagram of the multifunctional flexible tactile sensor for sensing external temperature information with (B) different temperature differences. (C) Comparison of infrared thermal images of the sensors touching metal, wood blocks, plastic, and ceramics at the same temperature. (D) Photographs of objects used for material recognition. (E) Comparison of the output voltage waveforms of flexible devices for objects made of different materials at the same temperature. (F) Confusion matrix result obtained from the decision tree model for material recognition. (G) Photographs of the array (4 × 4) assembled by the multifunctional flexible sensor. (H) Mapping results of shape recognition by the sensory array.

7. Qu, X., Liu, Z., Tan, P., et al. (2022). Artificial tactile perception smart finger for material identification based on triboelectric sensing. Sci. Adv. ***8***(31): eabq2521. https://doi.org/10.1126/sciadv.abq2521.
8. Ma, X., Wang, C., Wei, R., et al. (2022). Bimodal Tactile Sensor without Signal Fusion for User-Interactive Applications. ACS Nano ***16***(2): 2789–2797. https://doi.org/10.1021/acsnano.1c09779.
9. Liu, M., Zhang, Y., Wang, J., et al. (2022). A star-nose-like tactile-olfactory bionic sensing array for robust object recognition in non-visual environments. Nat. Commun. ***13***(1): 79. https://doi.org/10.1038/s41467-021-27672-z.
10. Pirozzi, S. (2020). Tactile Sensors for Robotic Applications. Sensors ***20***(24): 7009. https://doi.org/10.3390/s20247009.
11. Yuan, Z., and Shen, G. (2023). Materials and device architecture towards a multimodal electronic skin. Mater. Today ***64***: 165–179. https://doi.org/10.1016/j.mattod.2023.02.023.
12. Liu, F., Deswal, S., Christou, A., et al. (2022). Neuro-inspired electronic skin for robots. Sci. Robot. ***7***(67): eabl7344. https://doi.org/10.1126/scirobotics.abl7344.
13. Wu, F., Yu, P., and Mao, L. (2023). Neurotronics: Communicating with brain through chemically intelligent materials. The Innovation Materials ***1***(1): 100007. https://doi.org/10.59717/j.xinn-mater.2023.100007.

14. Wang, Y., Wu, H., Xu, L., et al. (2020). Hierarchically patterned self-powered sensors for multifunctional tactile sensing. Sci. Adv. ***6***(34): eabb9083. https://doi.org/10.1126/sciadv.abb9083.
15. Liu, W., Duo, Y., Liu, J., et al. (2022). Touchless interactive teaching of soft robots through flexible bimodal sensory interfaces. Nat. Commun. ***13***(1): 5030. https://doi.org/10.1038/s41467-022-32702-5.
16. Li, Y., Zhao, M., Yan, Y., et al. (2022). Multifunctional biomimetic tactile system via a stick-slip sensing strategy for human–machine interactions. npj Flex. Electron. ***6***(1): 46. https://doi.org/10.1038/s41528-022-00183-7.
17. Bao, R., Tao, J., Zhao, J., et al. (2023). Integrated intelligent tactile system for a humanoid robot. Sci. Bull. ***68***(10): 1027–1037. https://doi.org/10.1016/j.scib.2023.04.019.
18. Xu, Q., Qu, S., Ming, C., et al. (2020). Conformal organic–inorganic semiconductor composites for flexible thermoelectrics. Energy Environ. Sci. ***13***(2): 511–518. https://doi.org/10.1039/c9ee03776d.
19. Du, C., Cao, M., Li, G., et al. (2022). Toward Precision Recognition of Complex Hand Motions: Wearable Thermoelectrics by Synergistic 2D Nanostructure Confinement and Controlled Reduction. Adv. Funct. Mater. ***32***(36). https://doi.org/10.1002/adfm.202206083.
20. Lin, M., Zheng, Z., Yang, L., et al. (2022). A High-Performance, Sensitive, Wearable Multifunctional Sensor Based on Rubber/CNT for Human Motion and Skin Temperature Detection. Adv. Mater. ***34***(1): e2107309. https://doi.org/10.1002/adma.202107309.
21. Yang, W., Liu, H., Du, H., et al. (2023). Robust and superelastic spider web-like polyimide fiber-based conductive composite aerogel for extreme temperature-tolerant linear pressure sensor. Sci. China Mater. ***66***(7): 2829–2842. https://doi.org/10.1007/s40843-022-2418-1.
22. Xu, B., Ye, F., Chen, R., et al. (2022). A wide sensing range and high sensitivity flexible strain sensor based on carbon nanotubes and MXene. Ceram. Int. ***48***(7): 10220–10226. https://doi.org/10.1016/j.ceramint.2021.12.235.
23. Riazi, H., Taghizadeh, G., and Soroush, M. (2021). MXene-Based Nanocomposite Sensors. ACS Omega ***6***(17): 11103–11112. https://doi.org/10.1021/acsomega.0c05828.
24. Guo, X., Lu, X., Jiang, P., et al. (2022). $SrTiO_3$/CuNi-Heterostructure-Based Thermopile for Sensitive Human Radiation Detection and Noncontact Human–Machine Interaction. Adv. Mater. ***34***(35): e2204355. https://doi.org/10.1002/adma.202204355.
25. Ahmad, K., Mohammad, A., Mathur, P., et al. (2016). Preparation of $SrTiO_3$ perovskite decorated rGO and electrochemical detection of nitroaromatics. Electrochim. Acta ***215***: 435–446. https://doi.org/10.1016/j.electacta.2016.08.123.
26. Wan, X., Lu, X., Sun, L., et al. (2022). Interface-enhanced thermoelectric output power in CrN/SrTiO3– heterostructure. J. Energy Chem. ***64***: 16–22. https://doi.org/10.1016/j.jechem.2021.04.056.
27. Zou, X., Xu, Y., and Duan, W. (2021). 2D materials: Rising star for future applications. Innovation ***2***(2): 100115. https://doi.org/10.1016/j.xinn.2021.100115.
28. Wang, Z., Chen, M., Cao, Z., et al. (2022). MXene Nanosheet/Organics Superlattice for Flexible Thermoelectrics. ACS Appl. Nano Mater. ***5***(11): 16872–16883. https://doi.org/10.1021/acsanm.2c03813.
29. Liu, H., Chen, X., Zheng, Y., et al. (2021). Lightweight, Superelastic, and Hydrophobic Polyimide Nanofiber/MXene Composite Aerogel for Wearable Piezoresistive Sensor and Oil/Water Separation Applications. Adv. Funct. Mater. ***31***(13). https://doi.org/10.1002/adfm.202008006.
30. Yang, L., Li, Y., Fu, L., et al. (2023). Flexible pressure/temperature sensing system based on Te-PEDOT:PSS composite thermoelectric material. Sci. Sin. -Tech. ***53***(4): 487–498. https://doi.org/10.1360/sst-2022-0191.
31. Deng, Q., Huang, Y., Chen, B., et al. (2022). Conductive V_2C MXene and paralelectric $SrTiO_3$ containing polymer composites with high dielectric constant. Colloids Surf. A Physicochem. Eng. Asp. ***632***: 127763. https://doi.org/10.1016/j.colsurfa.2021.127763.
32. Wang, L., Zhang, M., Yang, B., et al. (2020). Highly Compressible, Thermally Stable, Light-Weight, and Robust Aramid Nanofibers/Ti(3)AlC(2) MXene Composite Aerogel for Sensitive Pressure Sensor. ACS Nano ***14***(8): 10633–10647. https://doi.org/10.1021/acsnano.0c04888.
33. Liu, J., Zhang, H.-B., Xie, X., et al. (2018). Multifunctional, Superelastic, and Lightweight MXene/Polyimide Aerogels. Small ***14***(45): e1802479. https://doi.org/10.1002/smll.201802479.
34. Zhao, L., Wang, L., Zheng, Y., et al. (2021). Highly-stable polymer-crosslinked 2D MXene-based flexible biocompatible electronic skins for in vivo biomonitoring. Nano Energy ***84***: 105921. https://doi.org/10.1016/j.nanoen.2021.105921.
35. Ballard, Z., Brown, C., Madni, A.M., et al. (2021). Machine learning and computation-enabled intelligent sensor design. Nat. Mach. Intell. ***3***(7): 556–565. https://doi.org/10.1038/s42256-021-00360-9.
36. Zhou, Z., Chen, K., Li, X., et al. (2020). Sign-to-speech translation using machine-learning-assisted stretchable sensor arrays. Nature Electronics ***3***(9): 571–578. https://doi.org/10.1038/s41928-020-0428-6.
37. Shih, B., Shah, D., Li, J., et al. (2020). Electronic skins and machine learning for intelligent soft robots. Sci. Robot. ***5***(41): eaaz9239. https://doi.org/10.1126/scirobotics.aaz9239.
38. Sundaram, S., Kellnhofer, P., Li, Y., et al. (2019). Learning the signatures of the human grasp using a scalable tactile glove. Nature ***569***(7758): 698–702. https://doi.org/10.1038/s41586-019-1234-z.
39. Li, Y., Yang, L., Deng, S., et al. (2023). A machine learning-assisted multifunctional tactile sensor for smart prosthetics. InfoMat ***5***. https://doi.org/10.1002/inf2.12463.
40. Shu, S., Wang, Z., Chen, P., et al. (2023). Machine-Learning Assisted Electronic Skins Capable of Proprioception and Exteroception in Soft Robotics. Adv. Mater. ***35***(18): e2211385. https://doi.org/10.1002/adma.202211385.
41. Niu, H., Yin, F., Kim, E.S., et al. (2023). Advances in flexible sensors for intelligent perception system enhanced by artificial intelligence. InfoMat ***5***(5). https://doi.org/10.1002/inf2.12412.
42. Wang, Y., Adam, M.L., Zhao, Y., et al. (2023). Machine Learning-Enhanced Flexible Mechanical Sensing. Nano-Micro Lett. ***15***(1): 55. https://doi.org/10.1007/s40820-023-01013-9.

ACKNOWLEDGMENTS

The authors acknowledge the Jiangxi Provincial Natural Science Foundation (20224ACB212001), the Youth Promotion Association of Chinese Academy of Science (2020320), the National Natural Science Foundation of China (62071462, 62071463), the National Science Fund for Distinguished Young Scholars of China (62125112), and the Suzhou Key Industrial Technology Innovation Project (SYG202029). The authors are grateful for the technical support from Nano-X Vacuum Interconnected Workstation of Suzhou Institute of Nano-Tech and Nano-Bionics, Chinese Academy of Sciences (SINANO).

AUTHOR CONTRIBUTIONS

T.L. and T.Z. are corresponding authors. S.H.D., T.L., and Y.L. conceived the idea, designed the experiments, and analyzed the data. T.L. modified the content of manuscript. Y.L. and J.B. contributed to the machine learning algorithms. T.L. and T.Z. supervised the whole project. All authors discussed the results and commented on the manuscript at all stages.

DECLARATION OF INTERESTS

The authors declare no competing interests.

SUPPLEMENTAL INFORMATION

It can be found online at https://doi.org/10.1016/j.xinn.2024.100596.

LEAD CONTACT WEBSITE

http://ting.sinano.ac.cn/